# Precursory slow slip and foreshocks on rough faults

**Camilla Cattania**[1] **and Paul Segall** [1]

[1]Department of Geophysics, Stanford University, Stanford, CA

**Key Points:**

- Rough fault simulations exhibit simultaneous foreshocks and creep caused by heterogeneity in normal stress induced by roughness
- Stress transfer between foreshocks and creep produces a positive feedback and 1/t acceleration prior to the mainshock
- The precursory phase is characterized by migratory seismicity and creep over an extended region

Corresponding author: Camilla Cattania, camcat@stanford.edu

**Abstract**

Foreshocks are not uncommon prior to large earthquakes, but their physical mechanism controversial. Two interpretations have been put forward: 1. foreshocks are driven by aseismic nucleation; 2. foreshocks are cascades, with each event triggered by earlier ones. Here we study seismic cycles on faults with fractal roughness at wavelengths exceeding the nucleation length. We perform 2-D quasi-dynamic simulations of frictionally uniform rate-state faults. Roughness leads to a range of slip behavior between system-size ruptures, including widespread creep, localized slow slip, and microseismicity.These processes are explained by spatial variations in normal stress ($\sigma$) caused by roughness: regions with low $\sigma$ tend to creep, while high $\sigma$ regions remain locked until they break seismically. Foreshocks and mainshocks both initiate from the rupture of locked asperities, but mainshocks preferentially start on stronger asperities. The preseismic phase is characterized by a feedback between creep and foreshocks: episodic seismic bursts break groups of nearby asperities, causing creep to accelerate, which in turns loads other asperities leading to further foreshocks. A simple analytical treatment of this mutual stress transfer, confirmed by simulations, predicts slip velocities and seismicity rates increase as $1/t$, where $t$ is the time to the mainshock. The model reproduces the observed migration of foreshocks towards the mainshock hypocenter, foreshock locations consistent with static stress changes, and the $1/t$ acceleration in stacked catalogs. Instead of interpreting foreshocks as either driven by coseismic stress changes or by creep, we propose that earthquake nucleation on rough faults is driven by the feedback between the two.

## Plain Language Summary

The occurrence of premonitory seismicity leading up to large earthquakes has been a central problem in seismology for several decades. In spite of constantly improving observational networks and data analysis tools, we are still grappling with the fundamental question: what causes foreshocks? Do they represent a chain of isolated events, or are they driven by slow slip over a large fault area, gradually accelerating before the mainshock? In this study, we tackle this question with numerical simulations of slip on a fault with a realistic (fractal) geometry. This geometrical complexity causes spatial variations in stress: compression or extension occur as irregularities on opposite sides of the fault are pressed closer together or further apart. This spatial heterogeneity modulates slip stability across the fault, causing simultaneous occurrence of slow slip and foreshocks. The two processes are linked by a positive feedback, since each increases stresses at the location of the other; under certain conditions, this can culminate in a large earthquake. Our model reproduces a number of observed foreshock characteristics, and offers new insights on the physical mechanism driving them.

## 1 Introduction

Foreshocks have been observed before many moderate and large earthquakes (Abercrombie & Mori, 1996; Jones & Molnar, 1976; Trugman & Ross, 2019; Ende & Ampuero, 2020), and even though modern seismic networks and analysis techniques have imaged foreshocks sequences in unprecedented detail (Ellsworth & Bulut, 2018; Tape et al., 2018), the physical mechanisms driving them remains debated (Gomberg, 2018; Mignan, 2014). One interpretation is that foreshocks represent failures of seismic sources (asperities) driven by an otherwise aseismic nucleation process (Tape et al., 2018; Bouchon et al., 2013, 2011; Schurr et al., 2014; N. Kato, 2014; Sugan et al., 2014; McGuire et al., 2005; Abercrombie & Mori, 1996). Aseismic acceleration prior to instability is predicted by theory (Ruina, 1983; Dieterich & Linker, 1992; Rubin & Ampuero, 2005; Ampuero & Rubin, 2008) and has been observed in laboratory experiments (Dieterich & Kilgore, 1996; McLaskey & Lockner, 2014; McLaskey, 2019) and numerical simulations (e.g. Dieterich & Linker, 1992; Lapusta et al., 2000; Lapusta, 2003). On the other hand, foreshocks have been interpreted as a cascade of events triggered by one another, not mediated by an aseismic process (Helmstetter & Sornette, 2003; Hardebeck et al., 2008). Recent studies have shown that the relative locations of foreshocks are in fact consistent with static stress triggering (Ellsworth &

Bulut, 2018; Yoon et al., 2019), and the lack of detectable aseismic slip preceding most moderate to large earthquakes supports the view of a triggering cascade.

The occurrence of foreshocks implies fault heterogeneity: if they are driven aseismically, heterogeneity leads to simultaneous occurrence of seismic and slow slip; in cascade model, it is required to explain why foreshocks remain small, while the mainshock evolves into a large rupture. Previous modeling studies of foreshocks have considered various sources of heterogeneity: velocity weakening asperities in a velocity strengthening fault (Dublanchet, 2018; Yabe & Ide, 2018); spatial variations in nucleation length on a velocity weakening fault caused by heterogeneous state evolution distance (Noda et al., 2013) or effective normal stress (Schaal & Lapusta, 2019). In these studies, aseismic slip can take place around the asperity due to either velocity strengthening behavior or frictional properties that lead to large nucleation dimensions; however, the presence of asperities with a small nucleation dimension can nevertheless lead to a cascade sequence (Noda et al., 2013).

Perhaps the most ubiquitous and best characterized source of heterogeneity is geometrical roughness: faults are fractal surfaces (Power et al., 1987, 1988; Power & Tullis, 1991; Sagy et al., 2007; Candela et al., 2009, 2012; Brodsky et al., 2016). Numerical and theoretical studies have shown that fault roughness has a first order effect on rupture nucleation (Tal et al., 2018), propagation and arrest (Fang & Dunham, 2013; Dunham et al., 2011; Heimisson, 2020).

Here we focus on the effect of long wavelength roughness (exceeding the nucleating length) on the nucleation phase and precursory seismicity leading up to a mainshock. We perform quasi-dynamic simulations of rough but otherwise uniform velocity-weakening faults embedded in a linear elastic medium. Numerical simulations show that a rich slip behavior ranging from slow slip to seismic ruptures arises as a consequence of normal stress heterogeneity induced by fault roughness, which causes spatial variations in strength and fault stability. Early in the cycle, low normal stress regions start to creep stably while high normal stress regions (from now on referred to as “asperities”) remain locked. The nucleation phase is characterized by an interplay between accelerating creep and episodic foreshocks: creep loads asperities, until they fail seismically; foreshocks increase stress on nearby asperities and creeping areas, causing the latter to accelerate in turn triggering subsequent foreshocks; asperities don’t fully relock after failure, gradually unpinning the fault and increasing the creeping area and velocities. We introduce a simple analytical model based on these interactions, which predicts acceleration in seismicity rate and creep as $1/t$, where $t$ is the time to the mainshock. Simulated sequences reproduce a number of observations, such as the relative location of foreshocks, their migration towards the mainshock hypocenter and the power-law acceleration of foreshocks in a stacked catalog.

## 2 Numerical model

We run 2-D plane strain simulations with the quasi-dynamic boundary element code *FDRA* (?, ?). The following equation of motion governs fault slip:

$$\tau_{el}(\mathbf{x}) - \tau_f(\mathbf{x}) = \frac{\mu}{2c_s} v(\mathbf{x}), \tag{1}$$

where $\mu$ is the shear modulus, $\tau_f$ the frictional resistance, and $\tau_{el}$ the shear stress due to remote loading and stress interactions between elements. The stress from each element is computed from dislocation solutions (e.g., Segall, 2010), accounting for variable element orientation. The right hand side is the radiation damping term, which represents stress change due to radiation of plane S-waves (Rice, 1993), with $c_s$ the shear wave speed. Earthquakes are defined as times when the slip velocity anywhere on the fault exceeds the threshold velocity $V_{dyn} = 2a\sigma c_s/\mu$ (Rubin & Ampuero, 2005), here $\sim 4$ cm/s.

Frictional resistance evolves according to rate-state friction (Dieterich, 1978):

$$\tau_f(v,\theta) = \sigma \left[ f_0 + a \log \frac{v}{v^*} + b \log \frac{\theta v^*}{d_c} \right], \tag{2}$$

where, $a$, $b$ and are constitutive parameters; $d_c$ is the state evolution distance; $\sigma$ is the effective normal stress; $v_0$ a reference slip velocity; $f_0$ the steady-state friction coefficient at $v = v^*$, and $\theta$ is a state-variable. Model parameters are listed in table 1. We employ the ageing law (Ruina, 1983) for state evolution:

$$\frac{d\theta}{dt} = 1 - \frac{\theta v}{d_c}, \tag{3}$$

such that steady-state friction at sliding velocity $v$ is

$$f_{ss}(v) = f_0 + (a-b) \log \frac{v}{v_0}. \tag{4}$$

We apply remote loading such that that the stress rate tensor is pure shear:

$$\dot{\sigma}_1 - \dot{\sigma}_3 \equiv \dot{\sigma}_D \tag{5}$$

$$\dot{\sigma}_1 + \dot{\sigma}_3 = 0, \tag{6}$$

where $\sigma_{1,3}$ are the principal stresses and $\sigma_D$ the differential stress. Resolving these on to the fault yields shear and normal stressing rates:

$$\dot{\tau} = \frac{\dot{\sigma}_D}{2} \sin(2\Psi + 2\theta) \tag{7}$$

$$\dot{\sigma} = \frac{\dot{\sigma}_D}{2} \cos(2\Psi + 2\theta), \tag{8}$$

where $\Psi$ is the average fault angle with respect to $\sigma_1$ and $\theta(x)$ the local slope. In general, both shear and normal stress vary in time; here we take $\Psi = 45°$, so that the spatially average normal stress is constant and equal to a uniform value $\sigma_0 = 10$MPa. In addition to the remote loading, slip on a rough fault causes normal stress changes, and normal stresses can locally become negative and induce opening if a purely elastic response is assumed. In contrast, tensile stresses are reduced or entirely inhibited in an elasto-viscoplastic medium with Drucker-Prager rheology. We approximate this behavior by setting a minimum value $\sigma_{min}$ for normal stress, $\sigma_{min} = 1$ kPa $\ll \sigma_0$.

The fault profile is fractal, characterized by power spectral density

$$P_h = C_h |k|^{-\beta} \tag{9}$$

with $\beta = 2H + 1$, where $H$ is the Hurst exponent. For natural faults this is typically between $0.4-0.8$ (Renard & Candela, 2017); here we set $H = 0.7$. For computational reasons, we only include wavelengths greater than 100m, close to the nominal nucleation length defined below, unless otherwise specified.

### 2.1 Model resolution

To correctly describe rupture behavior, both the nucleation length and the cohesive zone $\Lambda_0$ need to be well resolved (e.g. Lapusta et al., 2000; Perfettini & Ampuero, 2008). Erickson et al. (2020) found that a suite of planar fault models, including *FDRA*, produced well resolved simulations with $\Lambda_0/\Delta x \geq 3$, with $\Lambda_0 = \mu' d_c / b\sigma$ (Rubin, 2008), in agreement with previous studies (Day et al., 2005). A resolution of $\Lambda_0/\Delta x \approx 1.7$ produced similar temporal patterns, but slight differences in the frequency-magnitude distribution of simulated events. On a rough fault, normal stresses change with time and can locally be higher than the average, requiring a higher resolution. Moreover, we found that rough fault simulations are less forgiving than may expected from the results above.

**Table 1.** Model parameters

| Parameter | Value |
|---|---|
| a | 0.015 |
| b | 0.02 |
| $d_c$ | $10^{-4}$m |
| $\sigma_0$ | 10 MPa |
| $\dot{\tau}_0$ | 0.004 Pa s$^{-1}$ |
| $\mu$ | 30GPa |
| $\nu$ | 0.25 |
| $L_{min}$ | 100 m |
| $L$ | 5.2 km |
| $C_h$ | 0.013 |
| H | 0.7 |

For instance, a simulation resolving the nominal cohesive zone size with 4 grid points and a small fraction ($10-15\%$) of the fault with $\Lambda_0/\Delta x \approx 1-2$ produced abundant microseismicity and no full ruptures, while doubling the number of grid points generated full ruptures. Since earthquakes tend to arrest where $\sigma$ is high and the cohesive zone is small, a few under-resolved regions can determine the event size statistics. Here we use a nominal $\Lambda_0/\Delta x \approx 8$, and for the foreshock sequence discussed through most of the paper $\Lambda_0/\Delta x > 2$ everywhere. We tested a few individual foreshocks and verified that their rupture length does not change when doubling the resolution.

## 3 Summary of simulation results

The first order effect of fault roughness during the interseismic phase is a decrease in fault locking: as seen in Fig. 1(a), and previously noted by Tal et al. (2018), the maximum slip velocity on the fault is several orders of magnitude larger for a rough fault than for its planar counterpart. Fig. 1(b) shows that this is due to patches of higher velocity between locked patches. For simplicity, in the remainder of the paper we refer to these slowly slipping regions as "creeping", even though their slip velocity (estimated in section 4) can be several orders of magnitude lower than typically measurable fault creep.

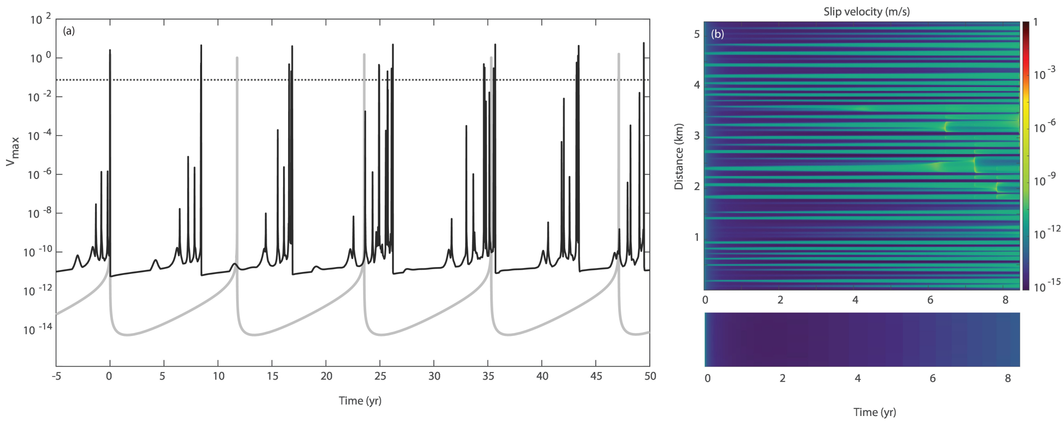


**Figure 1.** (a) Maximum slip velocity across multiple cycles on a rough (black) and comparable planar (grey) fault. The dotted line is the threshold velocity used to define earthquakes. (b) Slip velocity across the entire fault during one cycle showing alternating creeping and locked patches. The lower panel shows the slip velocity on a planar fault during the same time period (only a small region is shown, since velocity is effectively uniform).

During most of the interseismic phase the average slip velocity slowly increases, as creeping patches widen; this process is entirely aseismic, even though brief slow slip episodes with velocities up to about $10^{-6} - 10^{-5}$ m/s occur as creep fronts coalesce and break asperities (Fig. 1, 6−8 years into the cycle). Only in the final part of the cycle do asperities rupture in seismic events while creep rates increase (Fig. 2). During the acceleration leading up to the mainshock slip velocity on the fault does not increase gradually but in abrupt steps, associated with bursts of microseismicity. This pattern repeats at increasingly short temporal scales as the background slip velocity increases.

Foreshocks only occur once sufficient slip has accrued on the fault, and the first few sequences consist of single system-size ruptures. This is due to an increase in the amplitude of normal stress perturbations with total slip, quantified in Appendix A: microseismicity starts when the root-mean-square normal stress perturbation $\Delta\sigma_{rms}$ is of the order of the background normal stress $\sigma_0$. In the rest of the paper we will focus on one of the first sequences with foreshocks ($\Delta\sigma_{rms}/\sigma_0 = 1.1$), since later sequences, with more net slip, may not be well resolved (as discussed in 2). Other sequences are qualitatively similar (Supplementary Figure 1).

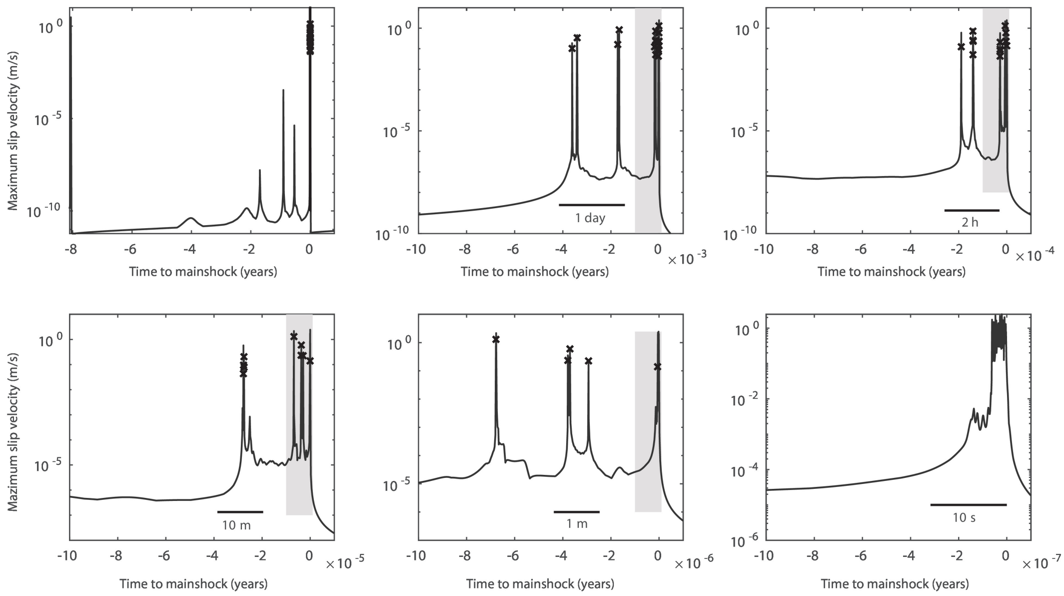


**Figure 2.** Average slip velocity on the fault leading up to the mainshock, showing a similar pattern across multiple temporal scales. Earthquakes are marked with crosses, and each grey box indicates the extent of the next panel.

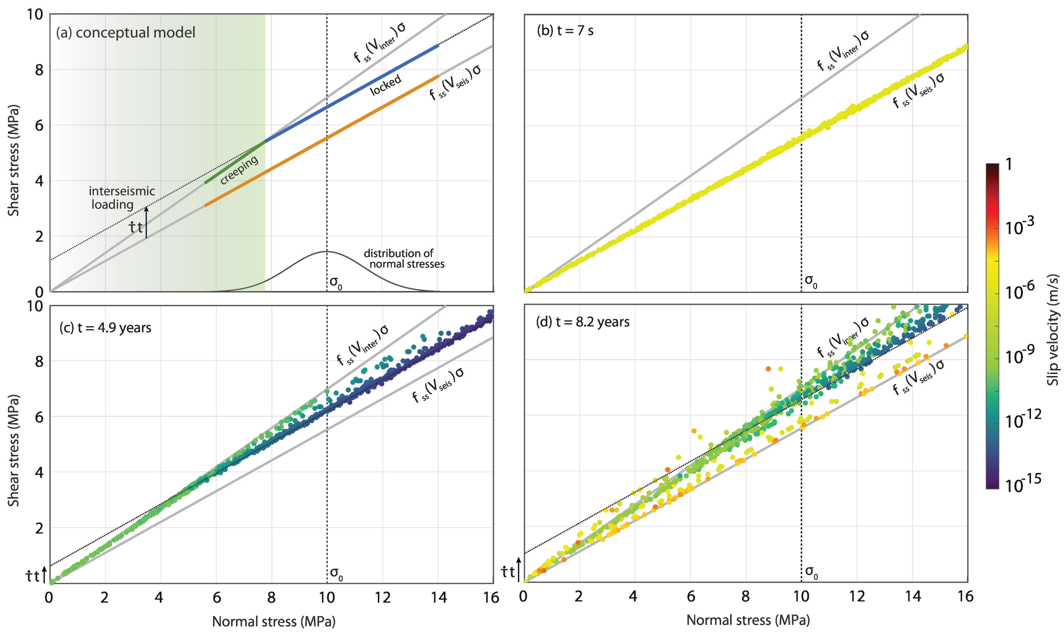


**Figure 3.** Conceptual model and simulation results for the evolution of stress on the fault. (a) Expected state of stress after the entire fault has ruptured (orange) and later in the cycle: points at low $\sigma$ reach the end of their cycle first and start creeping (green), while asperities are still locked (blue). $\sigma_0$ is the unperturbed normal stress, and the grey lines indicate the static and dynamic strength. (a-c) Shear and normal stresses from the simulation, right after an earthquake (b); during the aseismic phase of the cycle (c); towards the end of the nucleation phase (d).

## 4 Relationship between fault roughness and interseismic locking

Previous studies have shown that slip on a rough surface leads to perturbations in normal stress (Chester & Chester, 2000; Sagy & Lyakhovsky, 2019; Dunham et al., 2011). In Appendix A we summarize these findings and derive a simple expression for normal stress perturbations as a function of cumulative slip and fault topography. Normal stress perturbations on a fractal fault with uniform slip $S$ have a Gaussian distribution; for a fractal fault with Hurst exponent $H$, its standard deviation is given by

$$\Delta\sigma_{rms} = \frac{\mu' \alpha S}{2} \sqrt{\frac{H}{2-H}}\ (2\pi)^H\ k_{max}^{2-H}, \tag{10}$$

where $\mu' = \mu/(1{-}\nu)$ and $\nu$ is Poisson's ratio and $\alpha$ the roughness (section A1). These variations in normal stress are responsible for the occurrence of alternating creeping and locked regions, as shown in Fig. 4: creep takes place where roughness decreases the normal stress, while regions with increased $\sigma$ remain locked.

A simple model illustrating the heterogeneous response of a rough fault loaded at uniform rate is shown in Fig. 3. After a system-wide rupture, friction at all points on the fault is at steady-state $f_{co} = f_{ss}(V_{co})$, given by eq. 4 (this applies if fault healing occurs on a much longer timescale than the earthquake itself, as in the case of the ageing rate-state friction). As the fault is loaded at a uniform rate, points with low $\sigma$ reach static strength sooner than those at high $\sigma$ (Fig. 3(a)). A creeping patch may then become unstable if it exceeds a critical elasto-frictional length, or creep at constant stress otherwise. The steady-state velocity is $V_{cr} = \dot{\tau}/\kappa$, where $\kappa$ is the stiffness, which for a region of size $L$ is of the order of $L/\mu'$ so that $V_{cr} \approx L\dot{\tau}/\mu'$. The critical length for instability (nucleation length) was first estimated from a spring-slider linear stability analysis (Ruina, 1983); later, Rubin and Ampuero (2005) used energy balance arguments to derive expressions for ageing rate-state faults. In general, this critical length has the form

$$L_c = f(a,b)\frac{\mu' d_c}{\sigma} \tag{11}$$

where $f(a,b)$ is a function of rate-state parameters $a$, $b$; for rate-state friction with the ageing law and $a/b = 0.75$ (as in our case), $f(a,b) = b/[\pi(b-a)^2]$ and the nucleation length is denoted by $L_\infty$ (Rubin & Ampuero, 2005). Expressions for nucleation length derived for a homogeneous fault cannot directly be applied to an heterogeneous one. However, linear fracture mechanics can be used to derive alternative expressions for these cases, as done by Tal et al. (2018) for rough faults with small scale (sub-$L_c$) roughness, and Dublanchet (2018) for heterogeneous friction. With these caveats in mind, here we appeal to the concept of an heterogeneous nucleation length as an intuitive way to relate spatial variations in normal stress to slip behavior.

Due to the inverse proportionality between $L_c$ and $\sigma$, the first patches to reach static strength are the most stable ones (large $L_c$), thus favouring stable creep. During this phase we expect the average slip velocity on the fault to increase for several reasons: 1) the area of creeping patches increases as more points reach static strength, since the time to failure is given by $T_f \simeq \Delta\tau/\dot{\tau}$, where $\Delta\tau = [f_{ss}(V_{dyn}) - f_{ss}(V_{cr})]\sigma$ is the difference between the dynamic and "static" strength (Fig. 3); 2) Creep on low $\sigma$ patches redistribute stresses onto locked patches, contributing to the acceleration by causing points to be closer to failure than predicted from tectonic loading in Fig. 3(c); 3) The steady state slip velocity on each patch increases as it widens, since $V_{cr} \sim L_{cr}$. This leads to the interseismic acceleration seen in Fig. 1. As creep occurring in low $\sigma$ regions penetrate into asperities, it can cause them to fail in localized slow slip or earthquakes (velocity peaks in Fig. 1). Microseismicity occurs late in the cycle since the most locked patches, where the nucleation length is small enough to allow seismic rupture, are the last to reach failure.

## 5 Seismicity on strong patches

Foreshocks occur in subclusters at multiple temporal scales: Figs. 2 and 4 show 3 events occurring a few days before the mainshock, followed by quiescence and a second cluster about a day later; more clusters occur a few hours and a few minutes before the mainshock. Each burst represents the rupture of a group of nearby asperities (Fig 4 and Supplementary Figure), and the relative location of each event is consistent with static stress transfer from previous ones. This gives rise to migration (e.g. events 1-8, 9-14), which can also reverse due to repeated rupture of the same asperity (e.g. events no. 1,13,14 and 2,12,14 among others). A seismic cluster is bounded by stronger or wider asperities, which typically fail in later bursts: the increase in shear stress imparted by earthquakes on surrounding low $\sigma$ patches leads to a sudden acceleration, which in turn loads nearby asperities until they fail (see for example accelerated creep at the edge of previous foreshocks leading up to events 6, 11 and 14 in Fig. 4). Similarly, the mainshock initiates at the edge of the previous events and creep. The asperity on which it nucleates has a higher normal stress than nearby asperities and previous foreshocks.

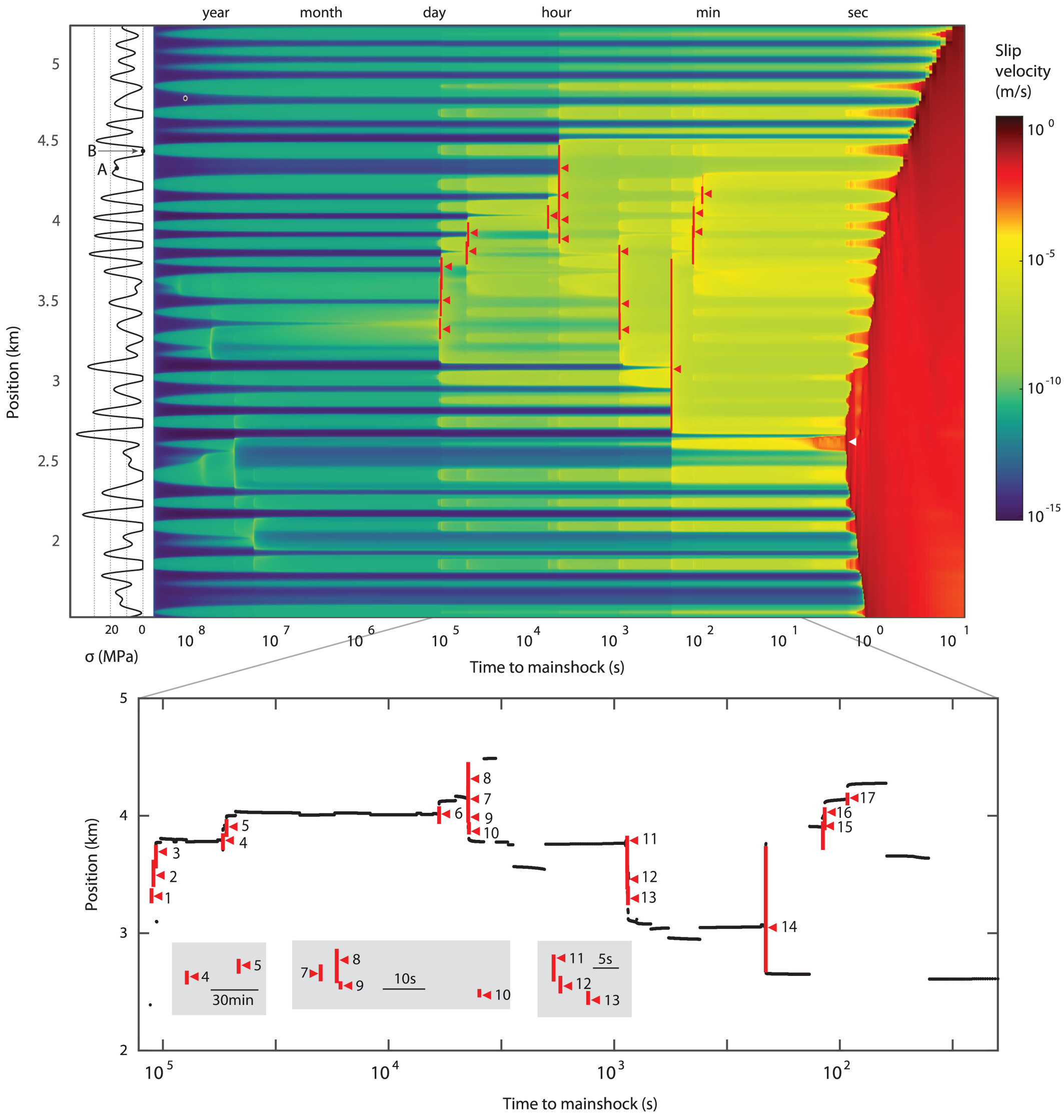


**Figure 4.** Creep acceleration and seismicity leading up to the mainshock. Top: slip velocity on the fault vs. time to the end of the mainshock, with red bars marking the rupture length and triangles marking the nucleation point (mid-point of the region where $v > V_{dyn}$ during the first earthquake time step). Note the sudden acceleration in nearby creeping patches and the widening of the fast slipping region with each successive seismic burst. Bottom: subset of the top panel, with events numbered by occurrence time. Small black dots indicate the location of maximum slip velocity at each time step, showing accelerated creep at the edges of each burst, where the subsequent ones initiate. Grey panels show close ups of a few clustered foreshocks.

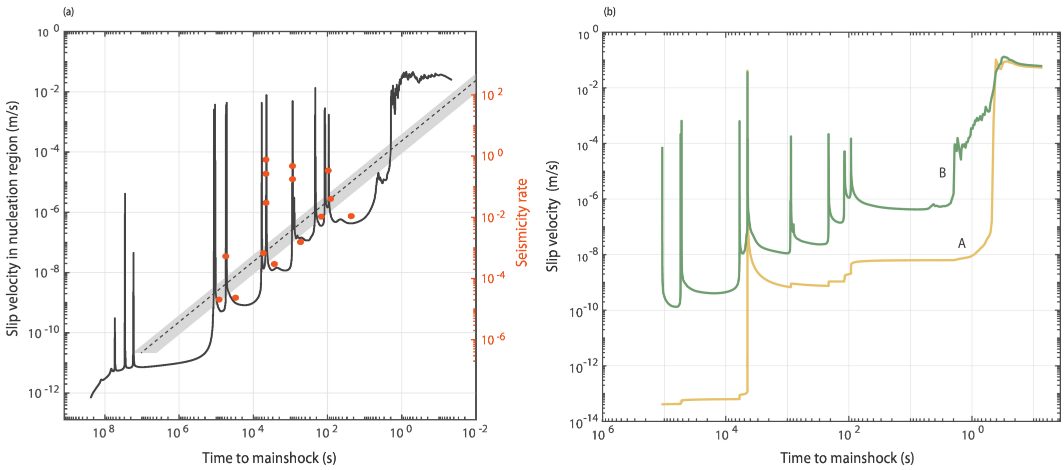


**Figure 5.** Slip velocity and seismicity rates during the foreshock sequence shown in Fig. 4. (Left) Black solid line: average slip velocity in the nucleation region vs. time to the end of the mainshock. Red circles: seismicity rates estimated by the inverse of intervent times, plotted at the midpoint between each pair of events. The y-axes are scaled with respect to one another according to eq. C1. The theoretical evolution of slip velocity (eq. 14) is indicated by the dotted line (for the median value of foreshock stress drop) and grey line (for the entire range of stress drops). (Right) Slip velocity vs. time for the asperity (A) and a nearby creeping patch (B).

In spite of the elevated normal stress on asperities, foreshocks don't have particularly high stress drops (0.1-2MPa): in agreement with Schaal and Lapusta (2019), who observed a similar behavior in 3-D simulations, we find that foreshocks are not confined to asperities, but propagate into the surrounding low $\sigma$ regions, thus lowering the average stress drop. The presence of such low stress-drop regions is also responsible for the partial overlap between consecutive events, even though in some cases asperities themselves rerupture (Fig. 4).

## 5.1 Feedback between creep and foreshocks

The average slip velocity during the foreshock sequence increases in sudden steps when asperities fail (Fig. 4, 5). The acceleration occurs even at large distances from the foreshocks compared to their rupture dimension, so that foreshocks contribute to widening the fast creeping area. Average slip velocities on the fault increase approximately with the inverse of time to mainshock (Fig. 5), similar to studies of velocity weakening asperities embedded in a velocity strengthening (creeping) fault (Dublanchet, 2018; Yabe &

Ide, 2018). However, neither asperities nor creeping patches follow this trend individually (Fig. 5).

To understand the effect of a seismic rupture on weak patches, consider the change in velocity caused by an instantaneous shear stress perturbation $\Delta\tau$ through the direct effect:

$$V = V_0 e^{\Delta\tau/a\sigma}, \tag{12}$$

where $V_0$ is the starting velocity. For a given stress change, areas at low normal stress are particularly susceptible to stress increases due to foreshocks, even if they are several rupture lengths away. As an example, Fig. 5(b) shows slip velocities on the asperity which ruptured in a foreshock (event no.8 in Fig. 4) and a nearby creeping patch, marked in Fig. 4. After the earthquake, the asperity does not fully relock, but continues slipping about 4 orders of magnitude faster than it did before. This behavior can be explained by the faster loading rate from the nearby creeping patches, which prevents the asperity from fully relocking. We can gain some intuition into this by treating the asperity as a spring-slider driven at a constant stressing rate, which in turn depends on the creep rate around it. The solution for velocity evolution derived in Appendix B predicts that the minimum slip speed right after an earthquake grows with stressing rate $\dot{\tau}$:

$$V_{lock} = V_{dyn} e^{b/a} \left( \frac{d_c \dot{\tau}}{b\sigma V_{dyn}} \right)^{b/a}. \tag{13}$$

After a mainshock, $\dot{\tau} \approx \dot{\tau}_0$ (the background loading rate); during the nucleation phase, creep velocities adjacent to the asperities increase (in this case, $V_{cr} \sim 1{\times}10^{-8}$m/s; see Fig.5), giving a stressing rate on the asperity of the order of $\tau_{cr} \approx \mu' V_{cr}/L_{asp} \approx \mu' V_{cr}/L_{min} = 4$Pa/s, here about $10^3$ times larger than the background loading rate $\dot{\tau}_0$. Plugging these numbers in the expression above, we expect $V_{lock}$ after the foreshock to be about $\sim 10^4$ times larger than its minimum value early in the cycle, consistent with the simulation (Fig. 5). The creeping patches and asperities subsequently decelerate, but the asperity slip velocity remains several orders of magnitude larger than before rupture (Fig. 4, 5).

The positive feedback between creep rates and seismicity rates leads to an overall acceleration and expansion of the creeping region. In Appendix C we derive a simple analytical model based on the observations described above. It relies on the following assumptions: 1. seismicity rate is proportional to average creep rate; 2. creep rates increase by a constant factor after each foreshock (derived from eq. 12), and don't change otherwise. This simple model predicts that the average slip velocity evolves as

$$\langle V \rangle = \frac{2L_{min}^2 \Delta\tau}{L\mu' \log(\beta)} \frac{1}{t_0 - t} \tag{14}$$

where $L$ is the dimension of the nucleation region, $\Delta\tau$ the foreshock stress drop and $\beta$ a factor quantifying the increase in creep velocity after each foreshock; $t$ is time since the first foreshocks and $t_0$ the time to instability, given by

$$t_0 = \frac{2L_{min}^2 \Delta\tau}{L\mu' \log(\beta) \langle V_0 \rangle}. \tag{15}$$

We estimated $\beta$ by applying eq. 12 to the creep patches in the nucleation region, and treating foreshocks as uniform stress drop cracks of fixed size, and we obtained values between 1.1−1.3 (the range is given by variability in foreshock stress drops). Overall, the average slip velocity in the nucleation region increases approximately as predicted by this expression (Fig. 5).

### 5.2 Stacked foreshock and aftershoc catalogs

The prediction of $1/t$ acceleration in creep rates and seismicity rates does not account for temporal clustering due to elastic interactions between asperities, visible in Fig. 5. Therefore, the $1/t$ acceleration in seismicity rates may not be readily visible in individual catalogs. To better capture temporal patterns, we stack the catalogs from all cycles. All foreshocks-aftershock sequences are shifted so the mainshock occurs at $t = 0$, and then combined in a single catalog. As shown in Fig. 6(a), the rate of foreshocks increases with the inverse time to the mainshock, as observed for stacked catalogs of natural sequences (Jones & Molnar, 1979; Ogata et al., 1995).

### 5.3 Onset of foreshocks and mainshock

The occurrence of foreshocks in the vicinity of the mainshock hypocenter raises the following question: why do some ruptures arrest, while others in the same region grow into large events? Fig. 4 shows that the mainshock, like most foreshocks, nucleates at the edge of a fast creeping region, on an asperity which arrested the previous event. The mainshock nucleation asperity has the highest normal stress on the entire fault. To verify whether other mainshocks also nucleate on high $\sigma$ asperities, we compare normal stresses in the nucleation region of mainshocks and nearby foreshocks. Fig. 7 shows that mainshocks tend to nucleate on stronger asperities than most of their foreshocks. This may

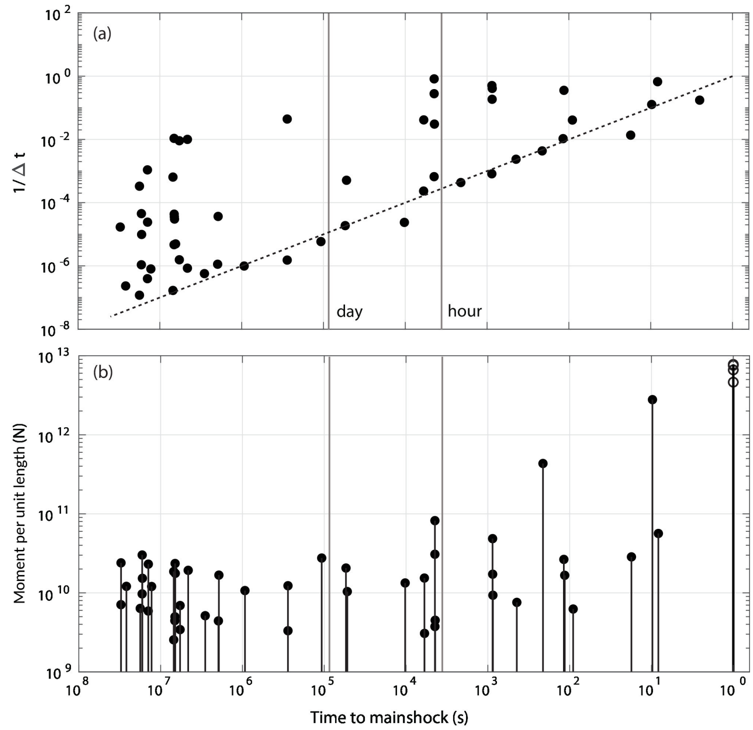


**Figure 6.** Moment per unit length and interevent times in the stacked catalog.(a) Seismicity rates estimated as the inverse of interevent time showing power-law acceleration. The dotted line is proportional to 1/t. (b) moment per unit length as a function of time to mainshock. Open circles indicate mainshocks.

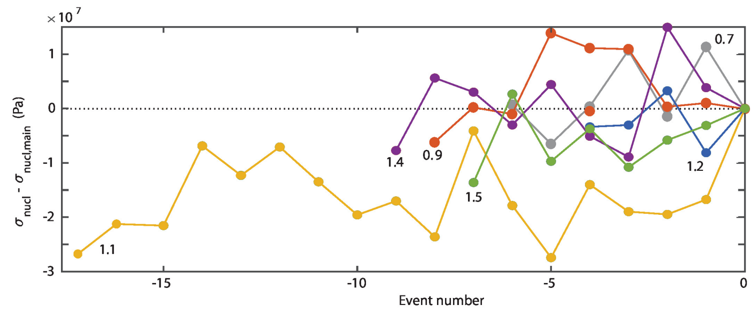


**Figure 7.** Difference between average normal stress in the nucleation region of foreshocks and their respective mainshocks. Nucleation is defined as the region between points exceeding a velocity threshold at the beginning of an earthquake (see section 2). We consider mainshocks all events with a rupture length exceeding 2km, and only select foreshocks within the mainshock rupture area. Numbers indicate $\Delta\sigma_{rms}/\sigma_0$ for each sequence.

not surprising in light of the simple model shown in Fig. 3, since patches with higher normal stress take longer to reach static strength. Once a strong asperity breaks, its stress drop is high and leads to a more pronounced stress concentration at its edge, allowing it to grow further than earlier events. This also explains why larger foreshocks tend to occur later in the cycle (Fig. 6(b)).

Rupture arrest is also determined by the strength of asperities ahead of the rupture tip, which act as barriers. We consider all asperities which are either within or adjacent to a rupture, and as expected we find that stronger asperities are more likely to arrest ruptures. We also find that a rupture nucleating at normal stress $\sigma_{nuc}$ has a 62% probability of breaking an asperity with normal stress exceeding $\sigma_{nuc}$, and a 77% chance of breaking an asperity with normal stress lower than $\sigma_{nuc}$. A selection bias could originate when grouping asperities according to this criterion: on average, asperities with $\sigma_{asp} > \sigma_{nuc}$ for a given earthquake are stronger than those with $\sigma_{asp} < \sigma_{nuc}$. However, we find that a difference remains when comparing asperities with approximately the same normal stress, indicating that $\sigma_{nuc}$ also affects rupture arrest.

## 6 Discussion

The results presented above show that the preseismic phase on a velocity-weakening fault with fractal roughness is characterized by a complex interplay between slow slip and foreshocks. Most of the period between mainshocks is devoid of seismicity, and characterized by localized patches of slow slip; late in the cycle, strong asperities start failing in short bursts, each of them in turn accelerating creep in its neighbourhood. This process leads to acceleration over an extended region (here about 20 times larger than the nominal nucleation dimension), with migration of seismicity towards the mainshock hypocenter.

### 6.1 Model limitations

The central result of this study is the coexistence and interaction of slow slip and foreshocks during nucleation on a rough fault. The primary control on this mixed behavior are normal stress perturbations due to roughness, and their effect on fault stability and slip patterns (section 4). These findings are not specific to rate-state (ageing law) friction, and likely apply for other frictional laws and weakening mechanism. On the other hand, certain simplifications in our study may be more consequential and deserve further investigation. The quasi-dynamic approximation can affect rupture arrest and foreshock rupture lengths, even though based on previous planar fault studies (Lapusta et al., 2000; Thomas et al., 2014) we don't expect the qualitative pattern to change dramatically with ageing-law rate-state friction. Considering the 3-dimensional nature of fault surfaces can modify certain aspects of fault dynamics, such the ability of an asperity to arrest rupture or the migration patterns caused by stress redistribution. Another significant assumption in our study is the purely elastic response: inelastic processes would limit the amplitude of stress perturbations, in particular at the smallest length scales (e.g. Dunham et al., 2011).

### 6.2 Conditions for foreshock occurrence

The dimension of asperities relative to characteristic elasto-frictional length scales is expected to affect foreshock behavior. Previous numerical studies of foreshocks on heterogeneous faults found that foreshocks only occur in a particular regime (Schaal & Lapusta, 2019; Dublanchet, 2018): asperities must be larger than the local nucleation dimension for seismic slip to occur, but smaller than a critical dimension (such as the nucleation dimension outside the asperity) to arrest without generating system-size ruptures. Here, the amplitude of spatial variations in $\sigma$ controls the range of local nucleation lengths $L_c$. As more slip accrues and normal stress perturbations grow, the nucleation length shrinks on the asperities and grows around them: therefore microseismicity only appears for sufficiently large normal stress perturbations (here $\Delta\sigma_{rms} \approx \sigma_0$).

A similar transition from few large ruptures to many smaller ones was found by Heimisson (2020) when increasing $k_{max}$; since the amplitude of normal stress perturbations grows with $k_{max}$ (eq. 10), this is consistent with our findings. Similarly, we expect that increasing fault roughness would have the same effect, since $\Delta\sigma_{rms}$ increase with the product of roughness and accrued slip. In our simulations, we chose $k_{max} \sim 2\pi/L_\infty$, for computational efficiency. To verify the effect of smaller wavelengths, we run also simulations for a smaller domain and $k_{max}$ up to 4 times higher (Supplementary Figure 2). We find that the presence of sub-$L_\infty$ asperities leads to more frequent aseismic ruptures (similar to those in Fig. 1). Both seismic and aseismic failures contribute to a gradual unpinning of the fault, as described above. The temporal evolution of slip velocities, with an abrupt increase during bursts and an an overall $1/t$ trend, is similar to the previous case.

### 6.3 Preslip vs. nucleation on rough faults

In the “preslip” model, aseismic slip is generally understood to occur at the location of the mainshock hypocenter, reflecting the notion that seismic instabilities develop over a region of finite size, as predicted by spring-slider stability analysis (Ruina, 1983) or fracture mechanics arguments for a finite fault (e.g. Rubin & Ampuero, 2005). It is conceivable that heterogeneity *within* the nucleation region could lead to foreshocks driven by accelerating slip; however, our results favor a different interpretation. Here the large scale precursory accelerating slip is not mainshock nucleation in the classical sense: since slow slip occurs in stable low $\sigma$ patches which do not accelerate when subject to slow loading, it does not directly evolve into a seismic rupture. Instead, slow slip triggers smaller scale nucleation on locked asperities, which can remain small or grow into a mainshock.

A similar relationship between preslip and mainshock initiation in presence of heterogeneity has been has been inferred in laboratory experiments. McLaskey and Lockner (2014) observed acoustic emissions (analogous to foreshocks) and slow slip leading up to failure in a centimeter-scale laboratory sample, and noted that system-size ruptures begin as acoustic emissions, with local strength variations perhaps controlling whether they evolve into larger ruptures. Similarly, meter-scale experiments by McLaskey (2019) show evidence of abrupt earthquake initiation caused by creep penetration from weak regions into a locked patches, “igniting” large ruptures.

The migratory behavior of microseismicity, and the earthquake hypocenter on the edge of the creeping region, also indicate of a different mechanism than self-nucleation. Recent observations of precursory slip leading up to glacial earthquakes by Barcheck et al. (n.d.) are similar to our results: slow slip and microseismicity migrate towards the mainshock hypocenter. Similar seismicity migration has also been observed prior to several events (Tohoku, 2011, A. Kato et al. (2012); Iquique, N. Kato (2014); Brodsky and van der Elst (2014); l’Aquila, Sugan et al. (2014)), and it is sometimes interpreted as evidence for aseismic slip.

On the other hand, migratory behavior can also be interpreted as evidence for direct triggering between foreshocks: seismicity prior to the 1999 Izmit (Ellsworth & Bulut, 2018) and 1999 Hector Mine (Yoon et al., 2019) exhibit a cascade behavior similar to what we observed here (Fig. 4): successive failure of neighbouring asperities, with each event nucleating at the edge of the previous ones, and in one case a rerupture of the same asperity (as in Fig. 4). Here we find that the migration is in some cases caused by direct stress triggering (leading to rapid failure of nearby asperities in a short burst), but it can also be mediated by accelerated creep between asperities.

An intriguing observation is the occurrence of earthquakes in the vicinity of a future mainshock hypocenter. The 2004 $M_w6$ Parkfield and the $M_w9$ Tohoku earthquakes were both preceded by moderate events within few years of the mainshock, a much shorter timescale than the respective earthquake cycles. Based on our results, which should be further verified with fully dynamic simulations, we suggest that local strength variations between potential nucleation patches within a small region may determine which earthquakes evolve into destructive events.

## 7 Conclusions

We find that fault roughness can lead to simultaneous occurrence of aseismic slip and foreshocks in the precursory phase of mainshocks, modulated by normal stress variations caused by fault geometry. The precursory phase can be described as a gradual unpinning of the fault by episodic asperity failure, mediated by aseismic slip. The creeping area widens and accelerates through each seismic burst, leading to migration of seismicity towards the eventual mainshock hypocenter. A simple model for the positive feedback between creep and seismicity predicts that slip accelerates as $1/t$, as confirmed by the simulations.

This process results in precursory slip on a larger scale than, and spatially distinct from, classical rate state nucleation on flat faults. Our results provide a physical interpretation for laboratory and field evidence of migratory preslip and foreshocks in the vicinity of a future mainshock hypocenter.

## Appendix A Normal stress variations

Here we derive the spatial distribution of normal stresses due to slip on a rough fault with small perturbations in elevation. Fang and Dunham (2013) derived the following expression for normal stress perturbations due to uniform unit slip:

$$\Delta\sigma(x) = \frac{\mu'}{2\pi} \int_{-\infty}^{\infty} \frac{y''(\xi)}{x - \xi} d\xi \tag{A1}$$

where $\mu' = \mu/(1-\nu)$ and compressive stresses are positive. The elevation profile can be written as

$$y(\xi) = \int_{k_{min}}^{k_{max}} \hat{y}(k)\ e^{ik\xi}\ dk \tag{A2}$$

Taking the second derivative and inserting into eq. A1 gives

$$\begin{aligned}\Delta\sigma(x) &= \frac{\mu'}{2\pi}\int_{-\infty}^{\infty}\frac{1}{\xi - x}\int_{k_{min}}^{k_{max}} k^2\hat{y}(k)\ e^{ik\xi}\ dk\ d\xi \\ &= \frac{\mu'}{2\pi}\int_{k_{min}}^{k_{max}} k^2\hat{y}(k)\ e^{ikx}\int_{-\infty}^{\infty}\frac{1}{u}\ e^{iku}\ du\ dk\ ,\end{aligned}$$

where $u = \xi - x$. We use the following results:

$$\begin{aligned}\int_{-\infty}^{\infty}\frac{\sin(kx)}{x}\ dx &= \pi \\ \int_{-\infty}^{\infty}\frac{\cos(kx)}{x}\ dx &= 0\ .\end{aligned}$$

Thus, the inner integral takes the value of $i\pi$ and

$$\Delta\sigma(x) = \frac{\mu' S}{2}\int_{k_{min}}^{k_{max}} k^2\hat{y}(k)\ e^{i(kx+\pi/2)}\ dk, \tag{A3}$$

where we have reinserted the total slip $S$. The integral has a form similar to the second derivative of the topography, but a phase shift of $\pi/2$ in each Fourier component. This result is consistent with the findings of (Romanet et al., 2019), who demonstrated that normal stress perturbations on a curved fault are proportional to the local curvature (which to first order is equal to the second derivative of the slope). The phase shift can be intuitively understood by considering a sinusoidal profile: a phase shift of $\pi/2$ places maximum compressive and tensile stresses at the inflection point of restraining and releasing bends (see in fig. A1). Since stress perturbations depend on the second derivative of the elevation profile, they are dominated by the shortest wavelengths.

### A1 Self-similar roughness

Consider a fault with a profile $y$ characterized by power spectral density

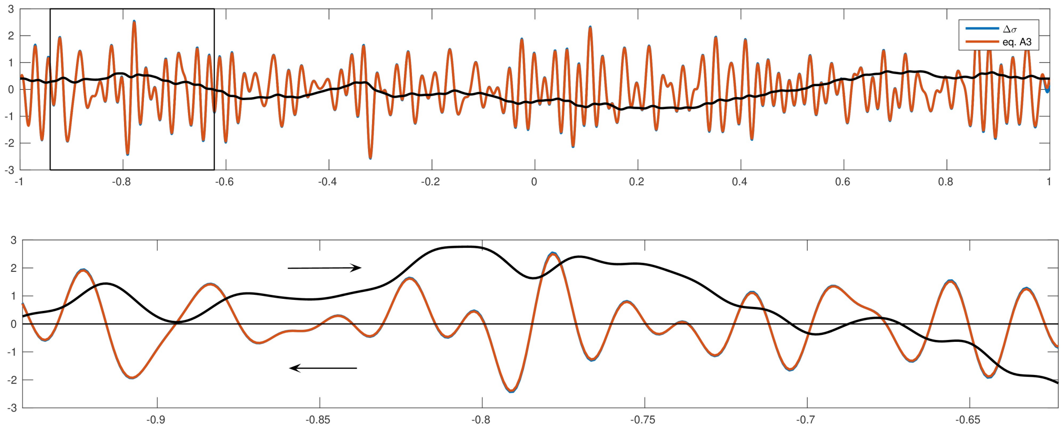


**Figure A1.** Top: Normal stresses from BEM calculations (blue) and eq. A3 (red), with unit slip and divided by $\mu'/2$. Black: fault profile rescaled by a factor of 500. Bottom: zoomed in (inset in top figure), with fault profile shifted and rescaled by 4000, showing normal stress perturbations corresponding to releasing and restraining bends.

$$P_h = C_h |k|^{-\beta} \tag{A4}$$

between $k_{min} = 2\pi/L$ and $k_{max}$, with $\beta = 2H + 1$ and $H$ the Hurst exponent. Using Parseval's theorem it can be shown that the root mean square elevation in the limit $k_{max} \gg k_{min}$ is

$$y_{rms} = \sqrt{\frac{C_h}{\pi(\beta - 1)}} \left(\frac{L}{2\pi}\right)^H = \alpha L^H \tag{A5}$$

where $\alpha$ is the surface roughness. Similarly, by applying Parseval's theorem to the second derivative of $y$ we obtain the the root mean square value:

$$y''_{rms} = \alpha \sqrt{\frac{H}{2 - H}}\, (2\pi)^H\, k_{max}^{2-H} \tag{A6}$$

Here we used fractal surfaces with random phases, resulting in a Gaussian distribution in $y(x)$ and $y''(x)$ is a Gaussian with standard deviation $y''_{rms}$ (e.g. Persson et al., 2005). Combining this result with eq. A3, we find that normal stress perturbations are Gaussian distributed with zero mean and standard deviation $\mu' S y''_{rms}/2$, where $S$ is the accrued slip.

## Appendix B Spring slider

To obtain the interseismic evolution of slip velocity, we consider a spring-slider with stiffness $\kappa$ driven at constant rate $\dot{\tau}_L$:

$$\frac{\tau_0 + t\dot{\tau}_L - \kappa\delta}{\sigma} = \left[\mu_0 + a\ln\left(V/V*\right) + b\ln\left(\theta V^*/d_c\right)\right] \ , \tag{B1}$$

where $\delta$ is the slip and $\tau_0$ is the stress at time $t = 0$ (see also Rubin and Ampuero (2005), eq.A12). Since we are interested in the velocity during the interseismic phase, the inertial term is not included. Time is measured since the last earthquake, and $\tau_0$ is the residual stress after rupture. More specifically, we define $t = 0$ as the moment when the system last crossed steady-state, and

$$\frac{\tau_0}{\sigma} = f + (a-b)\log\left(V_{dyn}/V^*\right) \tag{B2}$$

where $V_{dyn} = (2a\sigma/\mu)v_s$ is the velocity above which inertial effects play a role, in the no-healing regime (Rubin & Ampuero, 2005). Inserting eq. B2 into eq. B1 and solving for $V$ gives

$$V(t) = V_{dyn}\exp\left(\frac{t\dot{\tau}_L - k\delta}{a\sigma}\right)\left(\frac{d_c}{\theta V_{dyn}}\right)^{b/a} \tag{B3}$$

further assuming that the fault is locked ($k\delta/a\sigma \ll 1$) and far below steady-state ($\theta \sim t$), velocity evolves as

$$V(t) = V_{dyn}\exp\left(\frac{t\dot{\tau}_L}{a\sigma}\right)\left(\frac{d_c}{tV_{dyn}}\right)^{b/a} \ . \tag{B4}$$

The minimum velocity occurs at $t = b\sigma/\dot{\tau}_L$ and is given by

$$V_{lock} = V_{dyn}e^{b/a}\left(\frac{d_c\dot{\tau}_L}{b\sigma V_{dyn}}\right)^{b/a} \ . \tag{B5}$$

## Appendix C Preseismic acceleration

As discussed in section 5.1, the acceleration leading up to the mainshock is controlled by a feedback between creep in low normal stress patches and foreshocks on asperities. Here we develop a simple model of these interactions and the temporal evolution of acceleration.

Seismicity rate is controlled by the surrounding creep rate, which for simplicity we take as uniform. The interevent time on a single asperity is of the order of $\Delta\tau/\dot{\tau}$, where $\Delta\tau$ is the stress drop. Note that this expression does not apply if some interseismic slip takes place within the rupture area; however, Cattania and Segall (2019) obtained a similar expression, within a factor of order one, allowing for creep to penetrate the asperity. The overall seismicity rate on the fault is therefore $N\dot{\tau}/\Delta\tau$, where $N \approx L/L_{min}$ is the number of asperities in the nucleation region. During nucleation we can neglect tectonic loading, so $\dot{\tau} \approx \dot{\tau}_{cr} = \kappa V(t)$, with $\kappa \sim \mu'/2L_{min}$ so that the seismicity rate is

$$\frac{dn}{dt} = \frac{L\ \mu'}{2L_{min}^2 \Delta\tau}\langle V\rangle. \tag{C1}$$

where $n$ is the cumulative number of foreshocks, and $\langle V\rangle$ denotes average slip velocity. We further assume that each earthquake increases the average creep rate by a constant factor $\beta$, derived below, and we neglect self-acceleration of creeping patches. Slip velocities are then given by

$$\langle V(n)\rangle = \langle V_0\rangle\beta^n \tag{C2}$$

where $V_0$ is the average slip velocity before the first foreshock. Differentiating eq. C2 and combining with eq. C1 results in

$$\frac{d\langle V\rangle}{dt} = \frac{L\mu' \log(\beta)}{2L_{min}^2 \Delta\tau}\langle V\rangle^2 \tag{C3}$$

which has solution

$$\langle V\rangle = \frac{2L_{min}^2 \Delta\tau}{L\mu' \log(\beta)}\frac{1}{t_0 - t} \tag{C4}$$

where $t$ is time since the first foreshocks and $t_0$ the time to instability, given by

$$t_0 = \frac{2L_{min}^2 \Delta\tau}{L\mu' \log(\beta)\langle V_0\rangle}. \tag{C5}$$

Note that we assumed that the creep velocity remains high after each foreshock. For a creep patch of fixed dimension (stiffness) subject to a sudden stress increase, we would instead expect velocity to decay to the steady-state value determined by the background loading rate; however, simulations show that creep velocities remain high after each step (Fig. 4, 5), possibly due to the reduction in stiffness after each foreshock described in section 5.1.

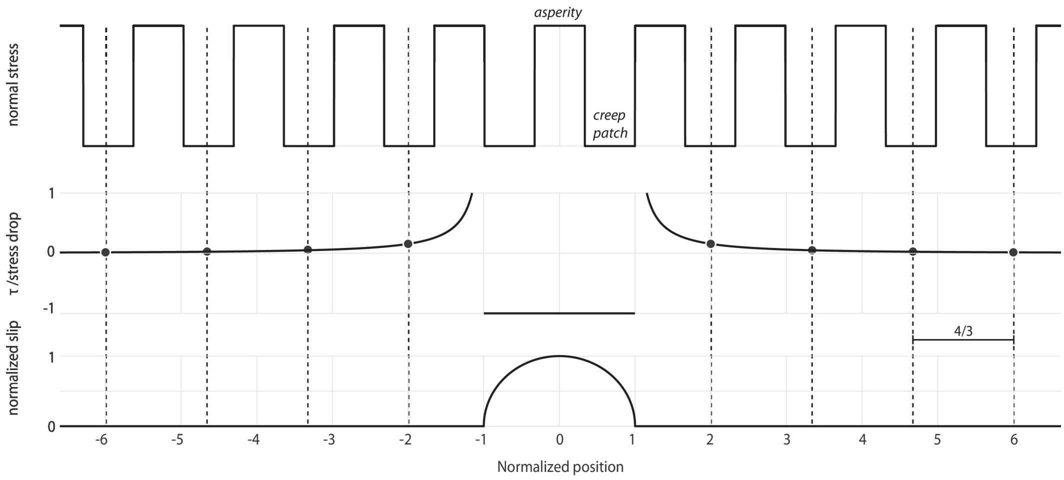


**Figure C1.** Simple model used to estimate changes in creep rate after a foreshock. Top: schematic spatial distribution of normal stress. Middle: shear stress change caused by a constant stress drop crack normalized by stress drop. Bottom: foreshock slip distribution. Dotted lines and circles indicate the center of creeping patches and locations at which stress changes are calculated.

The functional form of eq. C1 and C2 is not expected to change in 3D (even though $\alpha$ and the prefactor in eq. C1 will differ). Therefore we expect the main result of this analysis, which is the growth of velocity as the inverse of time to instability, to remain valid.

## C1 Estimating $\beta$

To obtain a rough estimate of $\beta$, the fractional change in creep rate due to a foreshock, we consider a simple model of periodic locked asperities alternating creeping patches, each region with length $2l$ (Fig. C1). We assume that asperities break in events with uniform stress drop, confined to a single asperity and the creeping patch on each side, with the next asperity acting as barrier. Since the response to stress changes is dominated by regions with low $\sigma$, we consider the change in velocity in creeping patches only.

The stress field outside a constant stress drop crack of length $2l$ and stress drop $\Delta\tau$ is (Bonafede et al., 1985):

$$\Delta\tau_{out} = \Delta\tau \frac{|x| - \sqrt{x^2 - l^2}}{\sqrt{x^2 - l^2}} \tag{C6}$$

where $x$ is the distance from the crack center. Since the system is symmetric around $x = 0$, in what follows we consider $x > 0$. We approximate the stress change within each creeping patch by the value at its center; as shown in Fig. C1, creeping patches are centered at positions $x = 2l, (2{+}4/3)l, (2{+}8/3)l, ....$ The stress change at position $x = nl$ is given by

$$\Delta\tau_{out} = \Delta\tau \frac{n - \sqrt{n^2 - 1}}{\sqrt{n^2 - 1}}. \tag{C7}$$

The local velocity after a stress step given by the direct effect is

$$V = V_0 \exp\left(\Delta\tau_{out}/a\sigma\right), \tag{C8}$$

where $V_0$ is the velocity before the stress step and $\sigma$ the normal stress in creeping patches. Assuming the same initial velocity $V_0$ in all creeping patches, the new average velocity is the sum of the velocity change in each patch divided by the total number of creeping patches $N_p$

$$\langle V \rangle = \frac{V_0}{N_p} \sum_{i=0}^{N_p - 1} \exp\left[\frac{\Delta\tau}{a\sigma}\left(\frac{n_i - \sqrt{n_i^2 - 1}}{\sqrt{n_i^2 - 1}}\right)\right], \tag{C9}$$

where $n_i = 2 + 4i/3$. The fractional change in slip velocity is simply $\beta = \langle V \rangle / V_0$ . At the onset of the foreshock sequence considered in the main text, slip velocities in creeping patches are of the order of $10^{-11}$m/s (as expected from $V_{cr} \sim \dot{\tau}/\mu' L_{cr}$), and their average normal stress is about 5 MPa. Foreshocks have stress drops between 0.1−2 MPa, with a median value of 0.5MPa. Considering the nucleation region between 1.7−4.7km (Fig. 4), the number of creeping patches is $\approx 3\text{km}/L_{min} = 30$; and since the analysis above only considers one side of the fault, $N_p = 15$. Plugging these values into eq. C9 gives $\beta$ between 1.1 and 1.3, depending on the stress drop.

## Acknowledgments

No data was used in this study. C.C. was funded by SCEC award no. 18166 and NSF award no. 1620496.

## References

Abercrombie, R. E., & Mori, J. (1996). Occurrence patterns of foreshocks to large earthquakes in the western United States. *Nature*, *381*(6580), 303–307. (ISBN: 0028-0836) doi: 10.1038/381303a0

Ampuero, J., & Rubin, A. (2008). Earthquake nucleation on rate and state faultsAging and slip laws. *Journal of Geophysical Research: Solid Earth*, *113*(August 2007), 1–61. doi: 10.1029/2007JB005082

Barcheck, G., Brodsky, E., Fulton, P. M., King, M. A., Siegfried, M. R., & Tulaczyk, S. (n.d.). Migratory earthquake precursors are dominant on a strain-energy limited ice stream fault. *Science Advances*.

Bonafede, M., Dragoni, M., & Boschi, E. (1985, December). Quasi-static crack models and the frictional stress threshold criterion for slip arrest. *Geophysical Journal International*, *83*(3), 615–635. doi: 10.1111/j.1365-246X.1985.tb04329.x

Bouchon, M., Durand, V., Marsan, D., Karabulut, H., & Schmittbuhl, J. (2013). The long precursory phase of most large interplate earthquakes. *Nature Geoscience*, *6*(4), 299–302. (Publisher: Nature Publishing Group) doi: 10.1038/ngeo1770

Bouchon, M., Karabulut, H., Aktar, M., zalaybey, S., Schmittbuhl, J., & Bouin, M. P. (2011). Extended nucleation of the 1999 Mw 7.6 Izmit earthquake. *Science*, *331*(6019), 877–880. (ISBN: 1095-9203 (Electronic)\r0036-8075 (Linking)) doi: 10.1126/science.1197341

Brodsky, E. E., Kirkpatrick, J. D., & Candela, T. (2016, January). Constraints from fault roughness on the scale-dependent strength of rocks. *Geology*, *44*(1), 19–22. (Publisher: GeoScienceWorld) doi: 10.1130/G37206.1

Brodsky, E. E., & van der Elst, N. J. (2014). The Uses of Dynamic Earthquake Triggering. *Annual Review of Earth and Planetary Sciences*, *42*(1), 317–339. doi: 10.1146/annurev-earth-060313-054648

Candela, T., Renard, F., Bouchon, M., Brouste, A., Marsan, D., Schmittbuhl, J., & Voisin, C. (2009). Characterization of fault roughness at various scales: Implications of three-dimensional high resolution topography measurements. *Pure and Applied Geophysics*, *166*(10-11), 1817–1851. (arXiv: 0810.1109 ISBN: 0033-4553) doi: 10.1007/s00024-009-0521-2

Candela, T., Renard, F., Klinger, Y., Mair, K., Schmittbuhl, J., & Brodsky, E. E. (2012). Roughness of fault surfaces over nine decades of length scales. *Journal of Geophysical Research: Solid Earth*, *117*(B8). (_eprint: https://onlinelibrary.wiley.com/doi/pdf/10.1029/2011JB009041) doi: 10.1029/2011JB009041

Cattania, C., & Segall, P. (2019). Crack models of repeating earthquakes predict observed moment-recurrence scaling. *Journal of Geophysical Research: Solid Earth*, *124*(1), 476–503. doi: 10.1029/2018JB016056

Chester, F. M., & Chester, J. S. (2000, October). Stress and deformation along wavy frictional faults. *Journal of Geophysical Research: Solid Earth*, *105*(B10), 23421–23430. doi: 10.1029/2000JB900241

Day, S. M., Dalguer, L. A., Lapusta, N., & Liu, Y. (2005). Comparison of finite difference and boundary integral solutions to three-dimensional spontaneous rupture. *Journal of Geophysical Research: Solid Earth*, *110*(B12). (_eprint: https://onlinelibrary.wiley.com/doi/pdf/10.1029/2005JB003813) doi: 10.1029/2005JB003813

Dieterich, J. H. (1978, July). Time-dependent friction and the mechanics of stick-slip. *pure and applied geophysics*, *116*(4), 790–806. doi: 10.1007/BF00876539

Dieterich, J. H., & Kilgore, B. (1996, April). Implications of fault constitutive properties for earthquake prediction. *Proceedings of the National Academy of Sciences*, *93*(9), 3787–3794. doi: 10.1073/pnas.93.9.3787

Dieterich, J. H., & Linker, M. F. (1992). Fault stability under conditions of variable normal stress. *Geophysical Research Letters*, *19*(16), 1691–1694. doi: 10.1029/92GL01821

Dublanchet, P. (2018, February). The dynamics of earthquake precursors controlled by effective friction. *Geophysical Journal International*, *212*(2), 853–871. doi: 10.1093/gji/ggx438

Dunham, E. M., Belanger, D., Cong, L., & Kozdon, J. E. (2011). Earthquake Ruptures with Strongly Rate-Weakening Friction and Off-Fault Plasticity , Part 2: Nonplanar Faults. *Bulletin of the Seismological Society of America*, *101*(5), 2308–2322. doi: 10.1785/0120100076

Ellsworth, W. L., & Bulut, F. (2018, July). Nucleation of the 1999 Izmit earthquake by a triggered cascade of foreshocks. *Nature Geoscience*, *11*(7), 531–535. doi: 10.1038/s41561-018-0145-1

Ende, M., & Ampuero, J. (2020, January). On the statistical significance of foreshock sequences in Southern California. *Geophysical Research Letters*, 2019GL086224. doi: 10.1029/2019GL086224

Erickson, B. A., Jiang, J., Barall, M., Lapusta, N., Dunham, E. M., Harris, R.,

. . . Wei, M. (2020, March). The community code verification exercise for simulating sequences of earthquakes and aseismic slip (SEAS). *Seismological Research Letters*, *91*(2A), 874–890. (Publisher: GeoScienceWorld) doi: 10.1785/0220190248

Fang, Z., & Dunham, E. M. (2013). Additional shear resistance from fault roughness and stress levels on geometrically complex faults. *Journal of Geophysical Research: Solid Earth*, *118*(7), 3642–3654. (ISBN: 2169-9356) doi: 10.1002/jgrb.50262

Gomberg, J. (2018, July). Unsettled earthquake nucleation. *Nature Geoscience*, *11*(7), 463–464. doi: 10.1038/s41561-018-0149-x

Hardebeck, J. L., Felzer, K. R., & Michael, A. J. (2008, August). Improved tests reveal that the accelerating moment release hypothesis is statistically insignificant: new tests contradict amr hypothesis. *Journal of Geophysical Research: Solid Earth*, *113*(B8). doi: 10.1029/2007JB005410

Heimisson, E. R. (2020, May). Crack to pulse transition and magnitude statistics during earthquake cycles on a self-similar rough fault. *Earth and Planetary Science Letters*, *537*, 116202. doi: 10.1016/j.epsl.2020.116202

Helmstetter, A., & Sornette, D. (2003, October). Foreshocks explained by cascades of triggered seismicity. *Journal of Geophysical Research: Solid Earth*, *108*(B10). doi: 10.1029/2003JB002409

Jones, L. M., & Molnar, P. (1976). Frequency of foreshocks. *Nature*, *262*.

Jones, L. M., & Molnar, P. (1979). Some characteristics of foreshocks and their possible relationship to earthquake prediction and premonitory slip on faults. *Journal Geophys. Res.*, *84*(9), 3596–3608.

Kato, A., Obara, K., Igarashi, T., Tsuruoka, H., Nakagawa, S., & Hirata, N. (2012). Propagation of slow slip leading up to the 2011 Mw9.0 Tohoku-Oki earthquake. *Science*, *335*, 705–709. doi: 10.1126/science.1215141

Kato, N. (2014). Deterministic chaos in a simulated sequence of slip events on a single isolated asperity. *Geophysical Journal International*, *198*(2), 727–736. doi: 10.1093/gji/ggu157

Lapusta, N. (2003). Nucleation and early seismic propagation of small and large events in a crustal earthquake model. *Journal of Geophysical Research*, *108*, 1–18. (ISBN: 2156-2202) doi: 10.1029/2001JB000793

Lapusta, N., Rice, J. R., Ben-Zion, Y., & Zheng, G. (2000, October). Elastodynamic analysis for slow tectonic loading with spontaneous rupture episodes on faults with rate- and state-dependent friction. *Journal of Geophysical Research: Solid Earth*, *105*(B10). (Publisher: John Wiley & Sons, Ltd) doi: 10.1029/2000JB900250

McGuire, J. J., Boettcher, M., & Jordan, T. H. (2005). Foreshock sequences and short-term earthquake predictability on east Pacific rise transform faults. *Nature*, *434*, 457–461.

McLaskey, G. C. (2019, December). Earthquake initiation from laboratory observations and implications for foreshocks. *Journal of Geophysical Research: Solid Earth*, 2019JB018363. doi: 10.1029/2019JB018363

McLaskey, G. C., & Lockner, D. A. (2014, August). Preslip and cascade processes initiating laboratory stick slip. *Journal of Geophysical Research: Solid Earth*, *119*(8), 6323–6336. doi: 10.1002/2014JB011220

Mignan, A. (2014, January). The debate on the prognostic value of earthquake foreshocks: a meta-analysis. *Scientific reports*, *4*, 4099. doi: 10.1038/srep04099

Noda, H., Nakatani, M., & Hori, T. (2013). Large nucleation before large earthquakes is sometimes skipped due to cascade-upImplications from a rate and state simulation of faults with hierarchical asperities. *Journal of Geophysical Research: Solid Earth*, *118*(6), 2924–2952. doi: 10.1002/jgrb.50211

Ogata, Y., Utsu, T., & Katsura, K. (1995, April). Statistical features of foreshocks in comparison with other earthquake clusters. *Geophysical Journal International*, *121*(1), 233–254. (tex.ids: Ogata1995 publisher: Oxford Academic) doi: 10.1111/j.1365-246X.1995.tb03524.x

Perfettini, H., & Ampuero, J.-P. (2008, September). Dynamics of a velocity strengthening fault region: Implications for slow earthquakes and post-seismic slip. *Journal of Geophysical Research*, *113*(B9), B09411. doi: 10.1029/2007JB005398

Persson, B. N. J., Albohr, O., Tartaglino, U., Volokitin, A. I., & Tosatti, E. (2005, January). On the nature of surface roughness with application to contact mechanics, sealing, rubber friction and adhesion. *Journal of Physics. Condensed Matter: An Institute of Physics Journal*, *17*(1), R1–R62. doi: 10.1088/0953-8984/17/1/R01

Power, W. L., & Tullis, T. E. (1991). Euclidean and fractal models for the description of rock surface roughness. *Journal of Geophysical Research: Solid Earth*, *96*(B1), 415–424. (_eprint: https://onlinelibrary.wiley.com/doi/pdf/10.1029/90JB02107) doi: 10.1029/90JB02107

Power, W. L., Tullis, T. E., Brown, S. R., Boitnott, G. N., & Scholz, C. H. (1987). Roughness of natural fault surfaces. *Geophysical Research Letters*, *14*(1), 29–32. (_eprint: https://onlinelibrary.wiley.com/doi/pdf/10.1029/GL014i001p00029) doi: 10.1029/GL014i001p00029

Power, W. L., Tullis, T. E., & Weeks, J. D. (1988). Roughness and wear during brittle faulting. *Journal of Geophysical Research: Solid Earth*, *93*(B12), 15268–15278. (_eprint: https://onlinelibrary.wiley.com/doi/pdf/10.1029/JB093iB12p15268) doi: 10.1029/JB093iB12p15268

Renard, F., & Candela, T. (2017). Scaling of fault roughness and implications for earthquake mechanics. In *Fault Zone Dynamic Processes* (pp. 195–215). American Geophysical Union (AGU). (Section: 10 _eprint: https://onlinelibrary.wiley.com/doi/pdf/10.1002/9781119156895.ch10) doi: 10.1002/9781119156895.ch10

Rice, J. R. (1993). Spatio-temporal complexity of slip on a fault. *Journal of Geophysical Research*, *98*(B6), 9885. (ISBN: 2156-2202) doi: 10.1029/93JB00191

Romanet, P., Sato, D., & Ando, R. (2019, November). Curvature, a mechanical link between the geometrical complexities of a fault. *arXiv:1911.02686 [physics]*. (arXiv: 1911.02686)

Rubin, A. M. (2008, November). Episodic slow slip events and rate-and-state friction. *Journal of Geophysical Research*, *113*(B11), B11414. (Publisher: John Wiley & Sons, Ltd) doi: 10.1029/2008JB005642

Rubin, A. M., & Ampuero, J. (2005). Earthquake nucleation on (aging) rate and state faults. *Journal of Geophysical Research*, *110*(2), 1–24. doi: 10.1029/2005JB003686

Ruina, A. (1983). Slip instability and state variable friction law. *J. Geophys. Res.*, *88*, 10359–10370. (ISBN: 0148-0227) doi: 10.1029/JB088iB12p10359

Sagy, A., Brodsky, E. E., & Axen, G. J. (2007). Evolution of fault-surface roughness with slip. *Geology*, *35*(3), 283–286. (ISBN: 0091-7613) doi: 10.1130/G23235A.1

Sagy, A., & Lyakhovsky, V. (2019). Stress patterns and failure around rough interlocked fault surface. *Journal of Geophysical Research: Solid Earth*, *124*(7), 7138–7154. doi: 10.1029/2018JB017006

Schaal, N., & Lapusta, N. (2019, February). Microseismicity on Patches of Higher Compression During LargerScale Earthquake Nucleation in a RateandState Fault Model. *Journal of Geophysical Research: Solid Earth*, *124*(2), 1962–1990. doi: 10.1029/2018JB016395

Schurr, B., Asch, G., Hainzl, S., Bedford, J., Hoechner, A., Palo, M., . . . Vilotte, J.-P. (2014). Gradual unlocking of plate boundary controlled initiation of the 2014 Iquique earthquake. *Nature*, *512*(7514), 299–302. (ISBN: 1476-4687) doi: 10.1038/nature13681

Segall, P. (2010). *Earthquake and Volcano deformation.* (Publication Title: Princeton University Press) doi: 10.1002/0471743984.vse7429

Segall, P., & Bradley, A. M. (2012). Slow-slip evolves into megathrust earthquakes in 2D numerical simulations. *Geophys. Res. Lett.*, *39*, 2–6. doi: 10.1029/2012GL052811

Sugan, M., Kato, A., Miyake, H., Nakagawa, S., & Vuan, A. (2014). The preparatory phase of the 2009 Mw 6.3 L'Aquila earthquake by improving the detection capability of low-magnitude foreshocks. *Geophysical Research Letters*, *41*(17), 6137–6144. doi: 10.1002/2014GL061199

Tal, Y., Hager, B. H., & Ampuero, J. P. (2018, January). The Effects of Fault Roughness on the Earthquake Nucleation Process. *Journal of Geophysical Research: Solid Earth*, *123*(1), 437–456. doi: 10.1002/2017JB014746

Tape, C., Holtkamp, S., Silwal, V., Hawthorne, J., Kaneko, Y., Ampuero, J. P., . . . West, M. E. (2018, July). Earthquake nucleation and fault slip complexity in the lower crust of central Alaska. *Nature Geoscience*, *11*(7), 536–541. doi: 10.1038/s41561-018-0144-2

Thomas, M. Y., Lapusta, N., Noda, H., & Avouac, J. P. (2014). Quasi-dynamic versus fully dynamic simulations of earthquakes and aseismic slip with and without enhanced coseismic weakening. *Journal of Geophysical Research: Solid

*Earth*, *119*(3), 1986–2004. (ISBN: 2169-9313) doi: 10.1002/2013JB010615

Trugman, D. T., & Ross, Z. E. (2019, August). Pervasive foreshock activity across Southern California. *Geophysical Research Letters*, *46*(15), 8772–8781. doi: 10.1029/2019GL083725

Yabe, S., & Ide, S. (2018, August). Variations in precursory slip behavior resulting from frictional heterogeneity. *Progress in Earth and Planetary Science*, *5*(1), 43. doi: 10.1186/s40645-018-0201-x

Yoon, C. E., Yoshimitsu, N., Ellsworth, W. L., & Beroza, G. C. (2019). Foreshocks and mainshock nucleation of the 1999 Mw 7.1 Hector Mine, California, earthquake. *Journal of Geophysical Research: Solid Earth*, *124*(2), 1569–1582. doi: 10.1029/2018JB016383